Analysis of residual cross sections from $^{14}N + ^{93}Nb$ reaction: Fusion dynamics of a non-α-cluster projectile

Himanshu Sharma,[1] Moumita Maiti,[1,*] T. N. Nag,[2] and S. Sodaye[2]
[1]*Department of Physics, Indian Institute of Technology Roorkee, Roorkee-247667, Uttarakhand, India*
[2]*Radiochemistry Division, Bhabha Atomic Research Centre, Mumbai-400085, India*

(Received 8 February 2023; revised 18 April 2023; accepted 22 May 2023; published 5 June 2023)

In the low-energy region, efforts have been made to understand the fusion mechanism of non-α-cluster projectiles, such as ^{14}N and ^{19}F. However, analyzing the contributing degrees of freedom has been hard in such reactions due to the lack of experimental data. This article reports the measurement of residual cross sections from the ^{14}N induced reaction on ^{93}Nb within the energy range of 42–59 MeV. The residues ^{104}Cd, ^{104}Ag, ^{103}Ag, ^{101}Pd, and ^{101m}Rh produced during the reaction were identified using γ-ray spectroscopy. The measured excitation functions have been analyzed with the equilibrium and pre-equilibrium mechanism-based model codes to understand the associated reaction mechanism. A revision of intensity corresponding to the 118.72 keV γ ray of ^{103}Ag has also been proposed in this article.

DOI: 10.1103/PhysRevC.107.064601

I. INTRODUCTION

Heavy-ion (HI) fusion study is one of the central topics of present-day nuclear reaction physics and has been extensively investigated in the last few decades due to the advancement in accelerator technologies [1]. The main objective of studying HI reactions is to learn about the processes involved and how they change with the entrance channel parameters, such as beam energy, angular momentum, and mass asymmetry. Projectile carries a large angular momentum and kinetic energy in HI reactions to overcome the Coulomb barrier. Peripheral and grazing collision lead to quasielastic (QE) (elastic, inelastic, or transfer) processes and deep inelastic collision (DIC). However, a clear separation between these two processes is yet to be found. If the projectile has an impact parameter less than the sum of radii of the interacting nuclei, substantial overlap between the interacting nuclei takes place, and a highly excited composite system is formed, further leading to pre-equilibrium (PEQ) emission, quasifission, fusion-evaporation, and fusion-fission. However, these processes have been independently studied, but their strength has not yet been fully evaluated below 10 MeV/A energy. Moreover, the importance of gaining substantial knowledge about processes such as nucleosynthesis [2], suppression of fusion cross section at energies above the barrier [3], fusion enhancement in the sub-barrier region [4], fusion hindrance in the deep sub-barrier region [5], and exploration of drip line extent of nuclear chart using radioactive ion beam [6], makes HI induced fusion an engrossing topic of modern nuclear research.

In the low-energy nuclear reactions ($E_{\rm lab} < 10$ MeV/A), the fusion mechanism dominates in which the compound nuclear process plays a significant role. A compound nucleus in an excited state primarily decays through the emission of neutrons, protons, α particles, γ rays, or nuclear fission. Thus, a wide range of excitation energies, spins, and intermediate nuclei encounter during the de-excitation of the compound nucleus. The level density of the final states and the barrier penetration factors are the fundamental components used in modeling the de-excitation based on statistical decay probabilities. The residues can be considered as the culmination of the processes mentioned above that could occur during the interaction of nuclei. Therefore, unraveling these processes and gaining a better understanding is crucial. The comparison of the measured residual excitation functions with the statistical model calculations would help to select essential parameters for the calculations.

Interestingly, tightly and loosely bound nuclei impact the interaction phenomenon differently. Strongly bound nuclei (^{12,13}C, ^{14}N, ^{16}O, ^{19}F, etc.) can transfer their full momentum to the target, resulting in complete fusion (CF). On the other hand, in weakly bound nuclei (like ^{6,7}Li), a sizable beam flux get divided into multiple fragments before fusing with the target [7–12]. Although complete fusion is expected to dominate below 10 MeV/A energy, the contribution from other processes, such as ICF and PEQ, has been reported for strongly bound projectiles in this energy region [13–22]. Furthermore, the dependency of fusion dynamics on entrance channel parameters, such as mass asymmetry, Coulomb factor ($Z_P Z_T$), α-Q value, etc., is not fully understood. A systematic study of those parameters is likely to aid in improving the existing reaction models and clarify the fusion dynamics at low energies.

Most of the experimental studies in the low energy region have been done using strongly bound α-cluster projectiles, like ^{12}C and ^{16}O [13–24]. A few studies have been reported using non-α-cluster projectiles like ^{14}N and ^{19}F on ^{175}Lu, ^{181}Ta, ^{159}Tb, ^{93}Nb, and ^{89}Y targets [25–31] to comprehend the fusion reaction dynamics in the medium mass region. Thus,

*Corresponding author: moumita.maiti@ph.iitr.ac.in

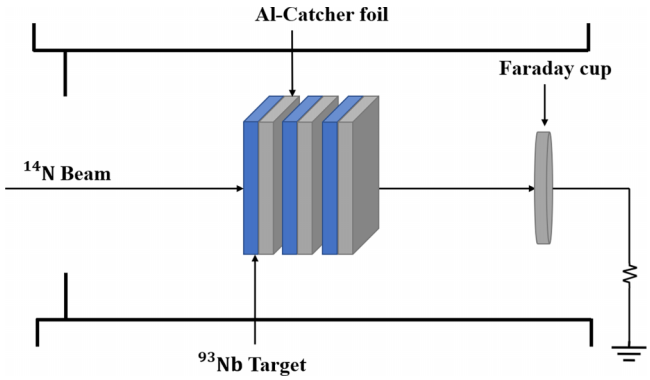

FIG. 1. A schematic diagram displays the target-catcher foil setup used for the examination of the ^{14}N-induced reaction on ^{93}Nb.

further experimental research is needed to comprehend the fusion reaction of non-α-cluster projectiles.

Our article reports in this endeavor an experimental study of $^{14}\mathrm{N}+{}^{93}\mathrm{Nb}$ reaction up to 59 MeV. Comprehensive data analysis was conducted to comprehend the reaction mechanisms and verify the accuracy of the model code parametrization. The article is organized as follows. The experimental method and the explanation of nuclear model calculations are outlined in Secs. II and III. The research findings are discussed in Sec. IV, and Sec. V summarizes the conclusions.

II. EXPERIMENTAL DETAILS

The experiment for the system $^{14}\mathrm{N}+{}^{93}\mathrm{Nb}$ was performed at the BARC-TIFR Pelletron facility in India. Self-supporting thin foils of spectroscopically pure (99.99%) niobium (^{93}Nb) of thickness 1.4 mg/cm^2 were prepared by the rolling technique. The arrangement depicted in Fig. 1 was adopted. The Nb and Al foils were mounted on an aluminum ring with an inner diameter of 12 mm and an outer diameter of 22 mm, with a thickness of 0.5 mm. The $^{14}\mathrm{N}^{5+}$-ion beam impinged on Nb targets backed by Al foils ($\approx$1.5 mg/cm^2 thickness) arranged in a stack. The total dose for each irradiation was determined by utilizing an electron-suppressed Faraday cup positioned at the back of the target setup. The aluminum foil was used to lower the energy and capture any recoils that may occur in the beam direction. The irradiation duration was determined by considering the beam intensity and the half-lives of the resulting radioactive isotopes. The energy loss in each foil was calculated using the stopping and range of ions in matter (SRIM) code [32]. The projectile's energy at the center of the target was estimated by averaging the incoming and outgoing beam energy.

After the end of the bombardment (EOB), the ^{93}Nb target and ^{27}Al catcher foils were analyzed through offline γ spectrometry using an HPGe detector in regular intervals to gauge the activity of the residues with the aid of a PC running the GENIE-2K software (Canberra). The energy resolution of the detector for 1332 keV γ ray of ^{60}Co was 2.0 keV, and it was calibrated using the standard sources, ^{152}Eu (13.506 y) and ^{60}Co (5.27 y) of known activity. The cross section of the evaporation residue at incident energy E was calculated using the following equation:

$$\sigma(E) = \frac{\lambda Y t_c}{\phi N_{tg}(1-e^{-\lambda t_i})(1-e^{-\lambda t_c})}. \quad (1)$$

The yield of evaporation residue (Y) at the EOB was determined using the equation

$$Y = \frac{C(t)}{\varepsilon^{\gamma} I^{\gamma}} e^{\lambda t_w}, \quad (2)$$

where $C(t)$ represents the count rate (number of counts per second). ε^{γ} and I^{γ} represent the efficiency of the detector and the branching intensity of the γ ray from the evaporative residue, respectively. λ represents the decay constant, and t_w is the cooling time. The incident beam flux is denoted as ϕ, the target nucleus areal density is N_{tg}, t_i is the time of irradiation, and t_c is the counting time. The data used to calculate the production cross sections of evaporative residues are listed in Table I.

TABLE I. Spectroscopic data [33,34] of the radionuclides produced in the $^{14}\mathrm{N}+{}^{93}\mathrm{Nb}$ reaction.

Residue	J^{π}	$T_{1/2}$	Decay mode (%)	E_{γ} (keV)	I_{γ} (%)
^{104}Cd	0^+	55.7 min	ϵ[a]+β^+ (100),	709.3	19.5
				559	6.3
^{104}Ag	5^+	69.2 min	$\epsilon+\beta^+$ (100),	767.7	65.7
				941.7	25
				857.9	10.4
				785.7	9.5
^{103}Ag	$7/2^+$	65.7 min	$\epsilon+\beta^+$ (100),	118.7	31.2
				266.9	13.3
				1273.8	9.3
				531.9	8.8
				243.9	8.5
^{101}Pd	$5/2^+$	8.47 h	$\epsilon+\beta^+$ (100),	296.3	19.0
				590.4	12.1
^{101m}Rh	$9/2^+$	4.34 d	ϵ (92.8), IT[b] (7.2),	306.9	81

[a]Electron capture.
[b]Isomeric transition.

The factors responsible for the uncertainty in the cross section measurement include (i) $\approx$2% error in the efficiency calibration of the detector, (ii) an approximate 2% error due to the nonuniformity of target thickness, and (iii) an uncertainty of $\approx$7% in the beam flux resulting from the variation in beam current. The measurement geometry was adjusted to keep the detector's deadtime $\leqslant$ 10%. Error in calculating beam energy due to energy loss as it passes through multiple target foils is also expected. However, the energy straggling effects are assumed minimal and not considered in the calculations. Moreover, the statistical error in the background-subtracted peak area count was considered in the error calculations. All the factors mentioned here were taken into account when estimating the error in the cross section calculation, and the average estimated error was $\approx$11%–14%. The estimated energy of the incident projectile at each foil carries an uncertainty factor, which comes from the error in the SRIM calculations.

III. MODEL CALCULATION

In this work, an attempt has been made to interpret the measured cross-section data of the residues produced in the $^{14}N + ^{93}Nb$ reaction within the 42–59 MeV incident energy range through the use of nuclear reaction model codes PACE4 [35] and EMPIRE-3.2.2 [36].

The foundation of PACE4 is the Hauser-Feshbach formalism, which tracks the coupling of angular momentum in each stage of the de-excitation of excited nuclei and deals with the equilibrium (EQ) emission process. The final state to which the nucleus will decay is decided by selecting a random number. The calculation involves a Monte Carlo method with a large number of events. This code considers the sequential emission of particles, one after the other, till it is energetically feasible. The Bass model [37] is employed for heavier projectiles to compute the fusion cross section and initial spin distribution. The partial cross section σ_ℓ for CN formation is given by

$$\sigma_\ell = \frac{\lambda^2}{4\pi}(2\ell + 1)T_\ell. \tag{3}$$

Here, λ is the wavelength, and ℓ is the angular momentum. The transmission coefficient T_ℓ is given by

$$T_\ell = \left[1 + \exp\left(\frac{\ell - \ell_{\max}}{\Delta}\right)\right]^{-1}. \tag{4}$$

Here, Δ is the diffuseness parameter, and $\ell_{\max}$ represents the maximum angular momentum, which is calculated from the total fusion cross section

$$\sigma_F = \sum_{\ell=0}^{\infty} \sigma_\ell. \tag{5}$$

The transmission coefficients for light particle (n, p, α) emission are realized by the optical model subroutine [38,39]. The code follows Fermi gas formalism for level densities in the calculation, with level density parameter $a = A/k$, where A is the mass number of the compound nucleus and k is a free parameter. The value of k used in the current calculations is 8. However, k could be varied to check the cross section dependency on its variation. The fission simulation as a decay mode is performed using the modified rotating liquid drop barrier by Sierk [40]. The probability of fission can be computed using Bohr and Wheeler formalism [41].

EMPIRE-3.2.2 code considers the EQ, PEQ, and direct nuclear processes. The Hauser-Feshbach model, which precisely links the angular momentum and parity of the emitted particles to the residual nucleus, is utilized in the EQ process. Additionally, width fluctuation correction is included (3 MeV HRTW (Hofmann, Richert, Tepel, and Weidenmueller) is used in the present calculations). For PEQ emission of particles, the algorithm can incorporate the traditional phenomenological exciton model. The differential cross section of PEQ emission can be determined as

$$\frac{d\sigma_{m,n}}{d\epsilon_n}(\epsilon_n) = \sigma^r_{m,n}(E_{\rm inc}) D_{m,n}(E_{\rm inc}) \times \sum_k W_n(E^*, k, \epsilon_n)\tau(k), \tag{6}$$

where $\sigma^r_{m,n}(E_{\rm inc})$ is the reaction cross section at incident energy $E_{\rm inc}$, $W_n(E^*, k, \epsilon_n)$ is the probability of emission of a particle of type n with energy ϵ_n from a state with k excitons and excitation energy E^* of CN, $\tau(k)$ is the lifetime of k exciton configuration, and $D_{m,n}(E_{\rm inc})$ is the depletion factor. The probability $W_n(E^*, k, \epsilon_n)$ is given by

$$W_n(E^*, k, \epsilon_n) = \frac{2s_n + 1}{\pi^2\hbar^3}\mu_n\epsilon_n\sigma_n^{\rm inv}(\epsilon_n) \times \frac{w_{\rm res}(p' - n, h', U^*)}{w_{cn}(p', h', E^*)} Q_b(p', h'), \tag{7}$$

where s_n, μ_n, and ϵ_n are the spin, reduced mass, and energy of nucleon. $E^*(U^*)$ is the excitation energy of CN (residual nucleus), $w(p', h', U^*)$ represents the particle-hole state density, which is calculated using the Williams formula [42], and $\sigma_n^{\rm inv}(\epsilon_n)$ stands for the inverse channel reaction cross section. $Q_b(p', h')$ encompasses the fraction of nucleons in the kth stage of the reaction.

A coupled channels approach or distorted wave Born approximation (DWBA) is utilized for direct processes. The CCFUS coupled channel code [43] was utilized to determine the HI fusion cross section, which separately considers inelastic excitations and transfer reactions. The exciton model with a mean free path parameter of 1.6 was utilized in this study. EMPIRE offers several models to account for level densities, like Gilbert-Cameron model (GCM) [44], generalized superfluid model (GSM) [45], and enhanced generalized superfluid model (EGSM) [46]. The GC model utilizes the constant temperature formula to calculate level density at low excitation energy and a Fermi gas model at high energy. The Fermi gas model (FGM) is the primary component of all these models, and its functional form is given by

$$\rho^{\rm FG}(E_x, J, \pi) = \frac{2J + 1}{48\sqrt{2}\sigma^{3/2}a^{1/4}U^{5/4}} \times \exp\left[2\sqrt{aU} - \frac{(J + 1/2)^2}{2\sigma^2}\right]. \tag{8}$$

Here, the level density parameter is denoted by a, the spin cutoff parameter is represented by σ^2, and the intrinsic level's spin and parity are indicated by J and π. To take into account the odd-even effects in nuclei, the excitation energy (E^*) is substituted with the effective excitation energy ($U = E_x - \Delta$), where Δ is closely related to the pairing energy. In the GC model, the level density parameter can be computed using the systematics outlined by Ignatyuk *et al.* [45], Young *et al.* [47], and Iljinov *et al.* [48]. The GSM is specified by a change in phase from a low-energy region to a high-energy region, with the critical excitation energy, U_c, marking the boundary between them. In GSM, the pairing correlations significantly impact the level densities at low energies where the superfluid behavior is prevalent. At high energies, the level densities are described using the FGM. For energies below U_c, the level densities are determined using the BCS model, and the superconducting pairing correlations are described through the correlation function. Like the GSM, the EGSM is built on the Fermi gas model level density, with an adiabatic mode and a collective enhancement factor that decreases with higher excitation energy and reaches unity above a

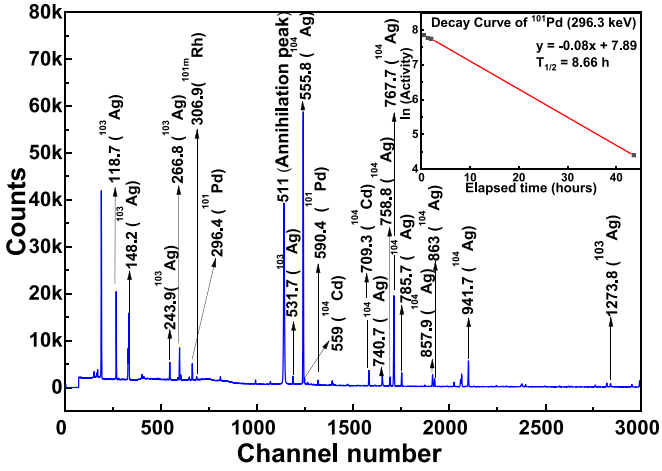

FIG. 2. A typical γ-ray spectrum of ^{93}Nb irradiated by $E_{\rm lab} = 50.9 \pm 1.6$ MeV ^{14}N beam, collected after 2.8 h of EOB. The γ-ray energies are in keV.

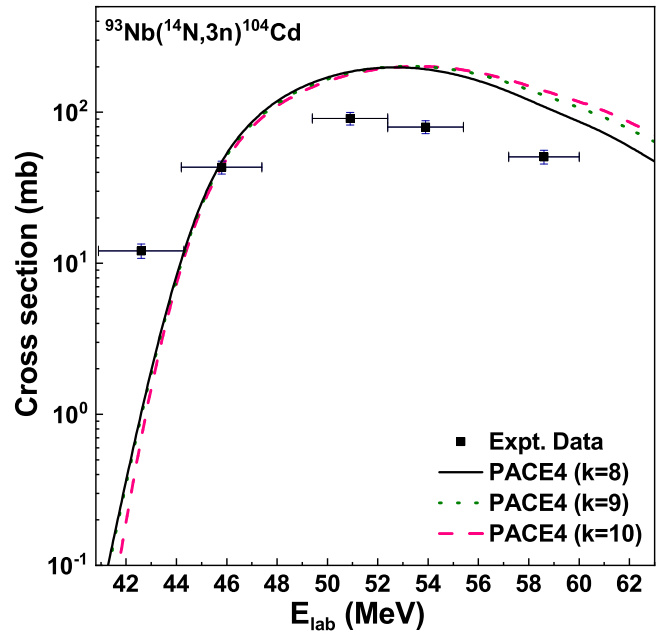

FIG. 3. Comparison of measured excitation function of ^{104}Cd with theoretical predictions from PACE4 at different k values.

certain critical temperature. In EGSM, the critical level density parameter is used below the critical temperature, and the Ignatyuk empirical level density parameter is applied above it. The transmission coefficients of particle emission have been calculated using the optical model. The input library RIPL-3 [49] contains the following internally provided information: nuclear masses, optical model parameters, ground state deformations, discrete levels and decay processes, level densities, fission barriers, and γ-ray strength functions. The optical model parameters for n and p are taken from Koning and Delaroche [50], for d from Haixia *et al.* [51], for t and ^{3}He from Becchetti and Greenlees [52], and for α particles from Avrigeanu *et al.* [53].

IV. DISCUSSION ON RESULTS

An examination of γ-ray spectra taken after the bombardment showed that the ^{14}N + ^{93}Nb reaction led to the production of ^{104}Cd, ^{104}Ag, ^{103}Ag, ^{101}Pd, and ^{101m}Rh residues in the target matrix within the energy range 42–59 MeV. A typical γ-ray spectrum, collected after 2.8 h, is shown in Fig. 2. The cross sections of the evaporative residues at different energies are shown in Table II.

A. *xn* channel

The effect of the variation of the choice of level density parameter $k = 8$, 9, and 10 on the cross section of ^{104}Cd produced via $3n$ channel in the ^{14}N + ^{93}Nb reaction is shown in Fig. 3. The figure clearly shows no meaningful disparity in the cross sections among the different k values. Also, the comparative analysis of other residues, such as ^{104}Ag and ^{103}Ag, found that $k = 8$ is the optimum value for this free parameter. Therefore, PACE4 with $k = 8$ has been used in the present calculations. Figure 4 displays the measured and calculated excitation functions of ^{104}Cd over the incident energy range of 41 to 63 MeV. The measured excitation function is underpredicted by the PACE4 calculations at lower energies (<46 MeV) and overestimated at higher energies (>46 MeV). The experimental data and EMPIRE with the three level-density models, GCM, GSM, and EGSM, all follow a similar trend. EMPIRE with GC level density reproduces the experimental data quite well within the uncertainties. EMPIRE with GSM and EGSM level densities underestimates the experimental cross section in the measured energy range. The difference in evaporation residue (ER) cross sections calculated using EMPIRE and PACE4 may be due to their use of different models. EMPIRE employs a simplified coupled channel approach (CCFUS), while PACE4 utilizes the one-dimensional barrier penetration model to calculate the fusion cross section. The disparity may also result from the fact that only the equilibrium mechanism is considered in the PACE calculations compared to the

TABLE II. Cross section (mb) of evaporation residues at various incident energies.

$E_{\rm lab}$ (MeV)	^{104}Cd	^{104}Ag	^{103}Ag	^{101}Pd	^{101m}Rh
58.6 ± 1.4	50.7 ± 5.4	96.1 ± 10.4	198.4 ± 20.2	55.4 ± 6.9	23.1 ± 5.4
53.9 ± 1.5	79.9 ± 7.8	115.3 ± 12.1	107.6 ± 11.6	54.4 ± 6.9	30.9 ± 10.2
50.9 ± 1.5	90.9 ± 8.8	123.7 ± 13.5	64.8 ± 7.2	48.8 ± 6.0	11.0 ± 3.8
45.8 ± 1.6	43.2 ± 4.2	41.6 ± 4.8	4.9 ± 1.0	13.2 ± 2.3	3.9 ± 2.5
42.6 ± 1.7	12.1 ± 1.3	11.6 ± 1.7	0.5 ± 0.1	3.8 ± 0.8	–

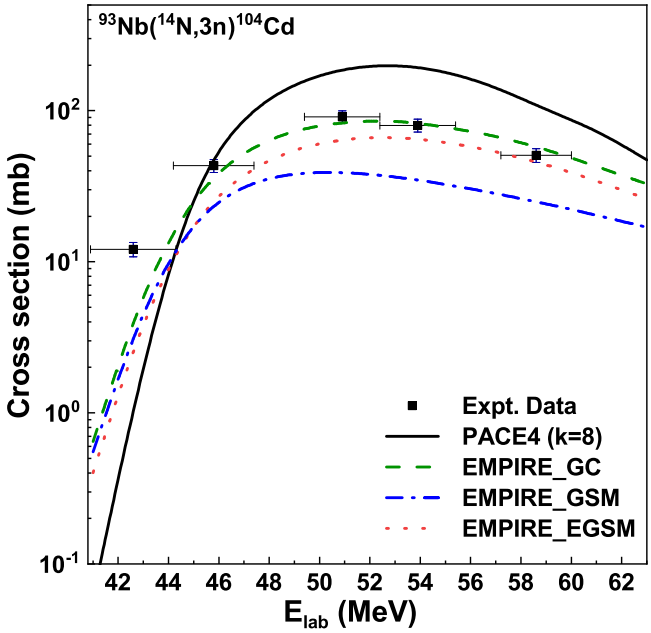

FIG. 4. Comparison of measured excitation function of ^{104}Cd with theoretical predictions from PACE4 and EMPIRE-3.2.2.

consideration of EQ and PEQ mechanisms in the EMPIRE calculations. The cross sections obtained from EMPIRE with GC level density display good agreement compared to those from PACE4 and EMPIRE with GSM and EGSM level densities.

B. *pxn* channel

^{104}Ag can be populated either independently via $p2n$ channel in the ^{14}N + ^{93}Nb reaction or through 100% ϵ and/or β^+ decay of ^{104}Cd. Both ^{104}Ag ($T_{1/2}$ = 69.2 min) and ^{104}Cd ($T_{1/2}$ = 55.7 min) have nearly the same half-lives. If the half-lives of the daughter nucleus (T_b) and parent nucleus (T_a) are nearly equal such that $T_a = T_b(1-\delta)$, then the activity ratio increases linearly with time as long as $t \ll 2\tau_b/\delta$, where t is the lapse time between the end of bombardment and the start of counting, τ_b is the mean lifetime of the daughter nucleus, and $\delta \ll 1$ [54]. To determine the independent cross section of ^{104}Ag, the production cross section of ^{104}Ag at an energy of 58.6 MeV is plotted at various times, as shown in Fig. 5(a), and then extrapolated to $t = 0$. Similarly, the independent cross sections of ^{104}Ag have been determined at other incident energies. The experimental data in the lower energy region (<51 MeV) are reproduced by EMPIRE within experimental uncertainties using GC and EGSM level densities, as demonstrated in Fig. 5(b). However, above 51 MeV incident energy, deviations are observed among the EMPIRE calculations. The results produced by the three level-density models in EMPIRE are consistent in the lower energy range, but they overestimate the measured data in the higher energy range. Except for the energy point, E_{lab} = 54 MeV, the experimental data are quite accurately predicted by PACE4 in the higher incident energy region ($E_{\rm lab}$ > 44 MeV). Since PACE4 calculations are based on Hauser-Feshbach formalism and do not account for the

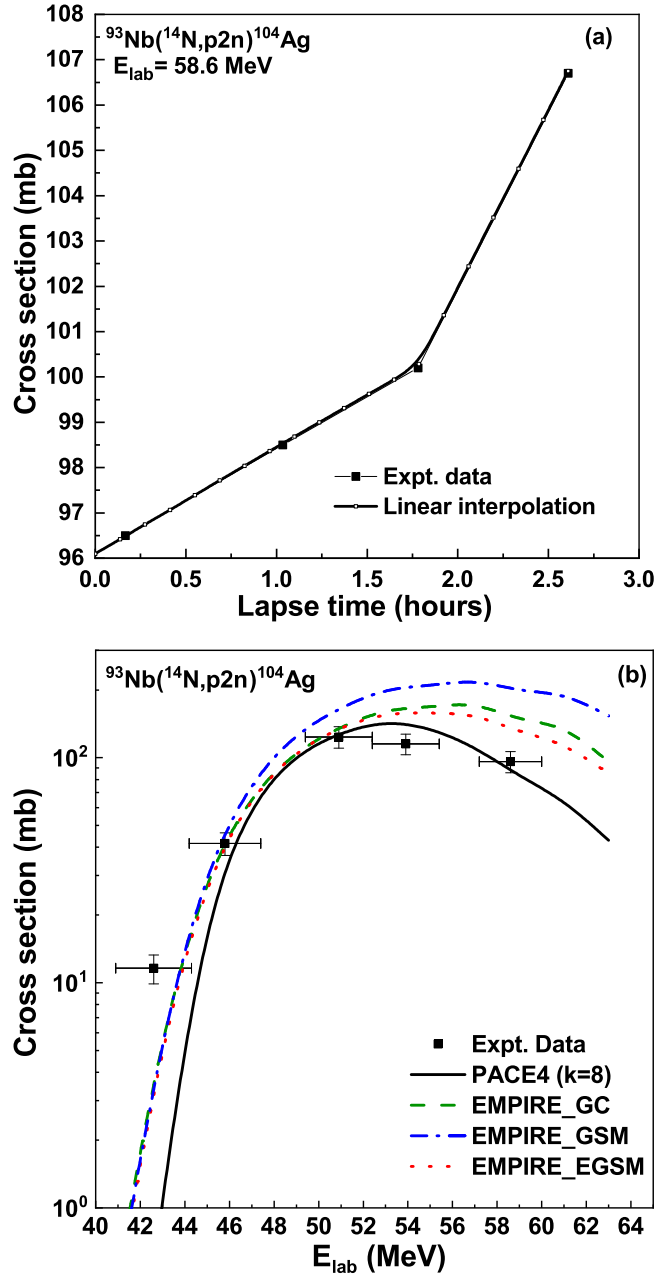

FIG. 5. (a) Cross section vs lapse time for ^{104}Ag. (b) Same as that of Fig. 4 for ^{104}Ag.

PEQ emission, the formation of ^{104}Ag can only be considered through the equilibrium mechanism.

Figure 6 shows the measured and calculated excitation functions of ^{103}Ag produced via the $p3n$ channel in the ^{14}N + ^{93}Nb reaction. This experiment identified the ground state of ^{103}Ag. Due to the short half-life of ^{103m}Ag (5.7 s) and ^{103}Cd (7.3 min), these residues could not be identified using the off-beam γ counting method. ^{103m}Ag decays 100% via isomeric transition and ^{103}Cd via ϵ and/or β^+ emission to ^{103g}Ag. Since $\lambda_{^{103m}\rm Ag} > \lambda_{^{103}\rm Cd} > \lambda_{^{103g}\rm Ag}$ (λ is the decay constant) and EMPIRE calculations also predict a good production of ^{103m}Ag and ^{103}Cd in the measured energy region, the

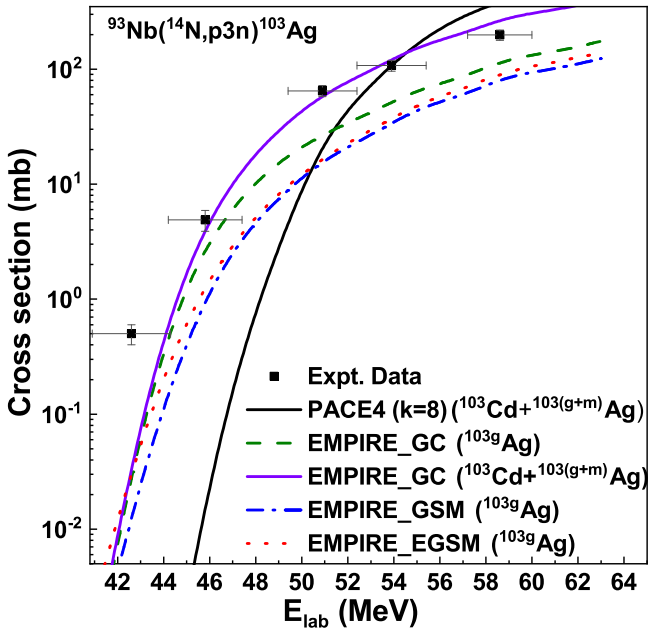

FIG. 6. Same as that of Fig. 4 for ^{103}Ag.

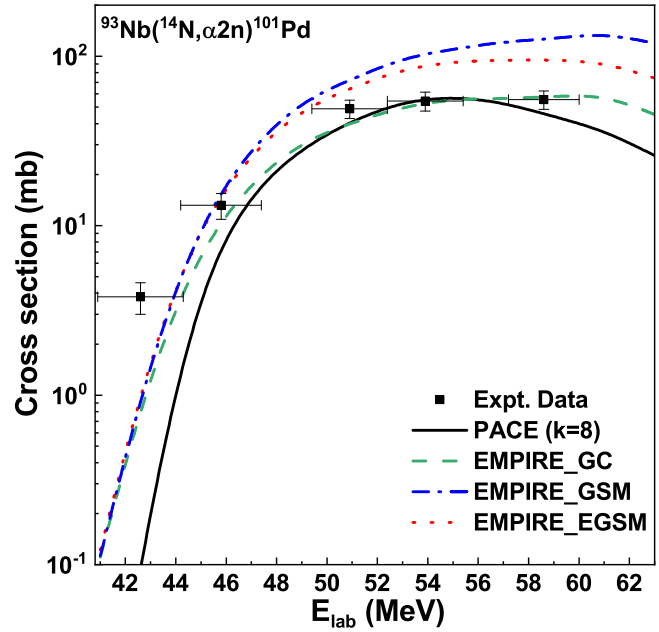

FIG. 7. Same as that of Fig. 4 for ^{101}Pd.

measured cross section of ^{103}Ag could be a combination of cross sections from its ground state and the decay of ^{103m}Ag and ^{103}Cd if they were produced. EMPIRE calculations with GC, GSM, and EGSM level densities for ^{103g}Ag underestimate the experimental data. Except for the highest energy point ($E_{\rm lab} = 59$ MeV), the cumulative excitation function of ^{103}Ag, which is obtained by combining the cross sections of ^{103}Cd, ^{103g}Ag, and ^{103m}Ag calculated using EMPIRE with GC level density, matches the experimental excitation function in the measured energy region. Thus, this experiment confirms the production of both ^{103}Cd and ^{103m}Ag. PACE4 underpredicts below $E_{\rm lab} = 54$ MeV and overestimates the experimental data above this energy.

C. αxn and αpxn channels

The measured and calculated excitation functions of ^{101}Pd produced via the $\alpha 2n$ channel in the ^{14}N + ^{93}Nb reaction are shown in Fig. 7. It can be seen that the measured cross sections follow a trend similar to the cross sections calculated using PACE4 and EMPIRE. Figure 7 shows that EMPIRE with GSM and EGSM level densities overestimate the measured cross section beyond 46 MeV incident energy while reproducing it below this energy. The EMPIRE model with GC level density follows the experimental data in the measured energy range within the uncertainty limits. Except for the highest energy point ($E_{\rm lab} = 59$ MeV), the measured cross section is predicted by PACE4 in the higher energy region ($E_{\rm lab} > 43$ MeV).

^{101m}Rh can be produced either independently via the αpn channel in the ^{14}N + ^{93}Nb reaction or through the decay of ^{101}Pd. Since the half-life of parent ^{101}Pd (8.47 h) is short than that of the daughter ^{101m}Rh (4.34 d), the cumulative cross section of ^{101m}Rh increases with time, as shown in Fig. 8(a). The independent cross section of ^{101m}Rh was also measured and is displayed in Fig. 8(b). Except for one energy point ($E_{\rm lab} = 54$ MeV), where the measured cross section agrees with EMPIRE (with EGSM and GSM) computations, the measured excitation function is quite well predicted by EMPIRE using the GC level density in the energy region $E_{\rm lab} > 46$ MeV.

A comparison between total fusion cross sections estimated using PACE4 and EMPIRE-3.2.2 has been done to clarify the discrepancy between theoretical predictions of cross sections and is presented in Fig. 9(a). At energies above 46 MeV, PACE4 and EMPIRE predictions have remarkably similar cross sections. Different cross sections are predicted by each model in the lower energy range, though. Except at 54 MeV and 59 MeV energies, experimental cross sections are well matched by EMPIRE calculations in the measured energy range and by PACE4 at energies higher than 43 MeV. This is attributed to the significant contribution of unidentified residues at high energies. The cross sections of these unidentified residues have been calculated using EMPIRE (with GC) and added to the measured cross sections of identified residues to get the total fusion cross section. The unmeasured residues ^{103}Cd ($4n$ channel), ^{104}Pd ($2pn$ channel), ^{103}Pd ($2p2n/\alpha$ channel), and ^{100}Pd ($\alpha 3n$ channel) are the ones that contribute the most to the total fusion cross section, as anticipated by theoretical calculations in the measured energy region. The half-lives and cross section of these ERs are listed in Table III. These residues were not detected due to the following reasons. The short half-life of ^{103}Cd made it challenging to observe, while the stability of ^{104}Pd prevented any detectable radiation emissions. ^{103}Pd was challenging to detect due to its low intensity γ line, and the production of ^{100}Pd could not be confirmed from the activity decay curve. Figure 9(b) compares the total fusion cross section (experimental data plus the cross section of unidentified residues predicted using EMPIRE with GC level density) with that computed using PACE4 and EMPIRE-3.2.2. The total fusion cross section begins to match

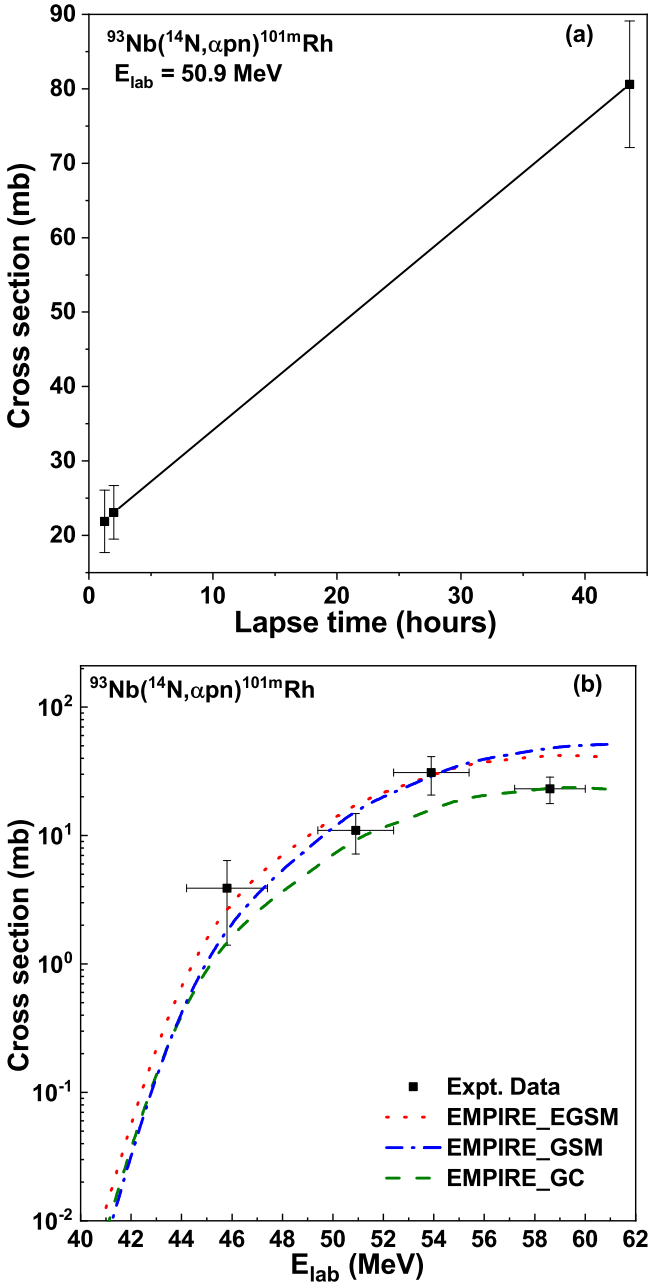

FIG. 8. (a) Cross section vs lapse time for ^{101m}Rh. (b) Same as that of Fig. 4 for ^{101m}Rh.

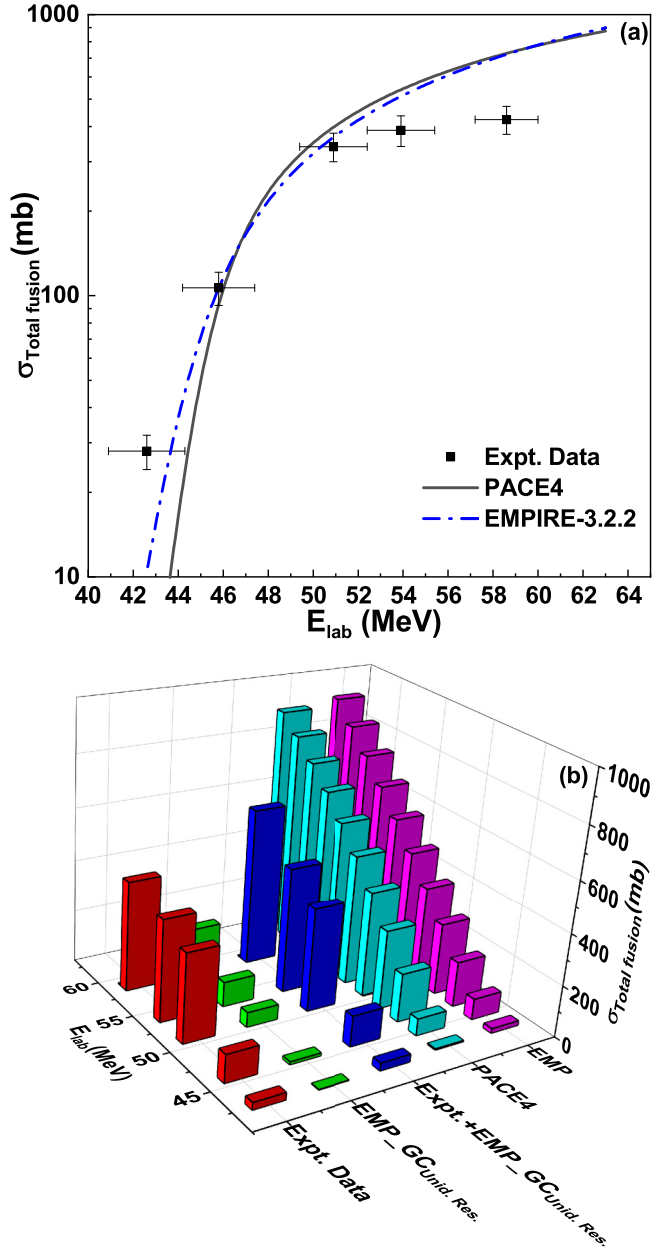

FIG. 9. (a) The calculated total fusion cross sections from model codes have been compared with the experimental measurement of residual cross sections, obtained by summing them up. (b) Total fusion cross section (experimental data + cross section of unidentified residues computed using EMPIRE with GC level density), in comparison to that calculated using PACE4 and EMPIRE-3.2.2. (The labels 'EMP' and 'Unid. Res.' represent 'EMPIRE' and 'Unidentified Residues', respectively.)

the EMPIRE and PACE calculations once the contribution of unmeasured nuclides is included.

D. Intensity determination of 118.72 keV γ ray of ^{103}Ag

Decay curves obtained from each characteristic γ-ray energy line of ^{103}Ag are shown in Fig. 10. It is worth mentioning that the activity at the EOB for the 118.72 keV (31.2%) γ line is distinct from the results obtained through the use of other lines [see the activity values (A) for different γ rays in Fig. 10]. The activity at the EOB for 118.72 keV (23.6%) γ line is close to the values obtained using other lines. It might be due to inaccuracy in the reported 118.72 keV γ-ray intensities. The activation formula can be used to compute the intensity corresponding to a specific γ line using the activity relation given by

$$A_{\mathrm{EOB}} = \frac{\lambda C_\gamma^1 e^{\lambda t_w}}{I_\gamma^1 \epsilon_\gamma^1 (1 - e^{-\lambda t_c})} = \frac{\lambda C_\gamma^i e^{\lambda t_w}}{I_\gamma^i \epsilon_\gamma^i (1 - e^{-\lambda t_c})}, \quad (9)$$

TABLE III. List of major unmeasured ERs during the experiment predicted by EMPIRE-GC.

Residue	Half-life	Cross section (mb) at E_{lab} 50.9 MeV	53.9 MeV	58.6 MeV
^{103}Cd	7.3 min	21.7	39.2	66.7
^{104}Pd	Stable	13.7	17.2	21.6
^{103}Pd	16.9 d	5.6	15.6	49.6
^{100}Pd	3.63 d	4.5	14.3	38.3

where the superscripts 1 and i signify the values related to the 118.72 keV and other γ lines of ^{103}Ag. C_γ represents the overall area counts, t_w and t_c are the waiting and counting times, λ is the decay constant, and ϵ_γ and I_γ refer to the efficiency and intensity for a specific γ line. For different γ's, only the net area counts under the peak, efficiency, and intensity differ. If the intensity of any other γ ray is known, it is possible to compute the intensity corresponding to a particular γ line using the relation

$$\frac{I_\gamma^1}{I_\gamma^i} = \frac{C_\gamma^1 \epsilon_\gamma^i}{C_\gamma^i \epsilon_\gamma^1}. \tag{10}$$

The intensity corresponding to the 118.72 keV line was estimated using this relation. Multiple activity measurements were performed over a sufficient period and in a fixed geometry on each activated target foil to monitor the decay profiles of the radionuclides. The 118.72 keV γ-peak intensity values obtained at each energy point were averaged to get the mean intensity value. Figure 11 depicts the estimated average experimental intensity value at different energies. The

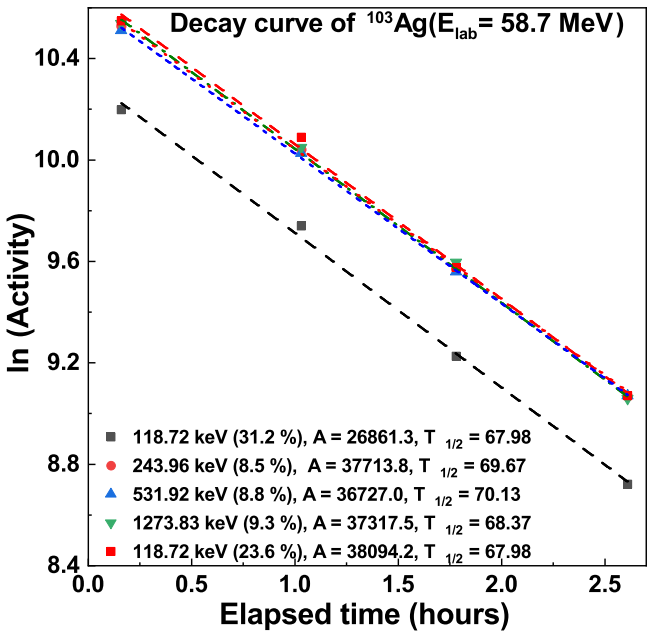

FIG. 10. Measured decay curves of ^{103}Ag using its different γ lines. The half-life is determined from the slope of a line fit to the data. The units of activity (A) and half-life ($T_{1/2}$) are in Becquerels and minutes, respectively.

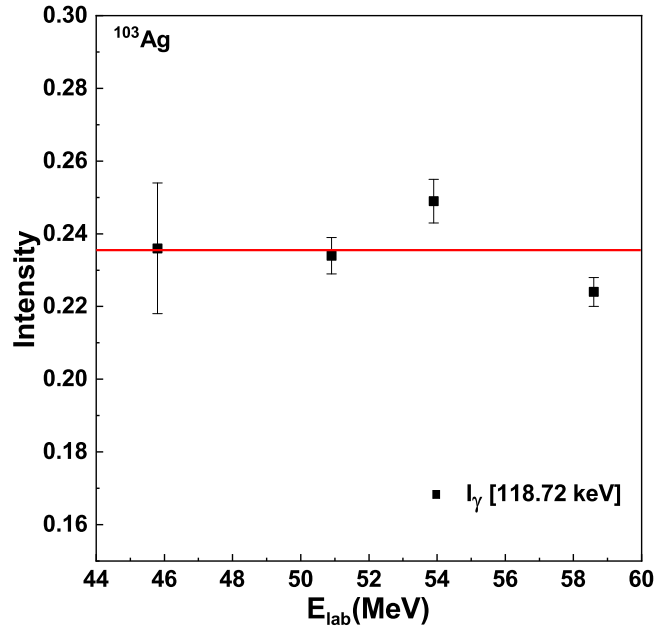

FIG. 11. Calculated γ-ray intensity of 118.72 keV peak of ^{103}Ag at different energy points.

overall average of intensity data is represented by the red line in Fig. 11, which comes out to be $23.6 \pm 0.8\%$, which differs from the values reported in different databases (31.2%). The calculated value is in proximity to the value reported in Misaelide's work (22.2%). Therefore, a dedicated experiment should be planned to determine a more precise and accurate value of the intensity of the 118.7 keV γ-ray from ^{103}Ag decay. The experimental intensity derived from the current analysis is presented in Table IV together with other reported intensities.

E. Nuclear potential parameters

Nuclear potential parameters like the Coulomb barrier height and barrier radius can also be inferred from the measured fusion cross section. In this work, the value of the Coulomb barrier and barrier radius has been deduced using the Wong formula [55]

$$\sigma_{CF} = \pi R^2 (1 - V_b/E_{c.m.}). \tag{11}$$

where V_b and $E_{c.m}$ are the Coulomb barrier and incident energy in the center-of-mass frame, respectively, and R is the interaction radius. The variation of the complete fusion cross

TABLE IV. Comparison between 118.72 keV γ-ray intensity and other values reported in different databases.

Database	E_γ (keV)	I_γ (%)
NuDat3.0 [33]	118.7	31.2 ± 0.20
LUND [34]	118.7	31.2 ± 0.07
NDS [56]	118.7	31.2 ± 0.20
JAEA [57]	118.7	31.2 ± 0.20
Misaelides's work [58]	118.7	22.2
Present work	118.7	23.6 ± 0.8

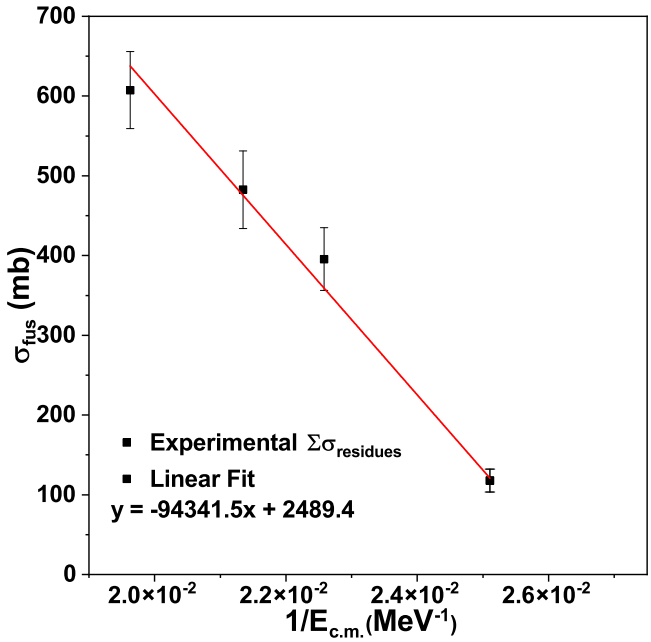

FIG. 12. The total fusion cross section (sum of measured cross sections of all residues + cross section of unidentified residues computed using EMPIRE with GC level density) plotted against the inverse of center-of-mass beam energy.

section as a function of $1/E_{\text{c.m.}}$ is displayed in Fig. 12. The Coulomb barrier and barrier radius has been extracted from the fitted straight line equation, $\sigma_{CF} = -94341.5/E_{\text{c.m.}} + 2489.4$. The value of the Coulomb barrier is found to be 37.9 ± 0.2 MeV, which is in the proximity of barrier height predicted by the Bass model ($V_C^{\text{Bass}} = 38.5$ MeV). The barrier radius obtained from the measured fusion cross section is 8.9 ± 0.3 fm. The calculated radius using the formula $R = R_0(A_P^{1/3} + A_T^{1/3})$, with A_P and A_T being the masses of the projectile and target and a constant value of $R_0 = 1.2$ fm, is 8.3 fm. This current measurement is close to the calculated value.

V. CONCLUSION

For the first time, cross sections of five residues, ^{104}Cd, ^{103}Ag, ^{103}Ag, ^{101}Pd, and ^{101m}Rh, from the ^{14}N + ^{93}Nb reaction within the 42–59 MeV energy range, were measured and analyzed in the framework of the compound and precompound nuclear theory, using statistical model codes PACE4 and EMPIRE-3.2.2. EMPIRE calculations with GC level density successfully reproduced the experimental data in most reaction channels. The cross section in the high energy region was pretty well anticipated by PACE4 simulations, demonstrating no PEQ emission in the $p2n$ channel. Following the EOB activity observed in other γ lines of the decay of ^{103}Ag, the estimated experimental intensity of the 118.72 keV γ line is 23.6 ± 0.8, differing from values listed in various nuclear databases. However, the revised intensity is close to the value reported in Misaelide's work. Nuclear potential parameters, like the Coulomb barrier height and barrier radius, have also been derived in this work and show good agreement with theoretical calculations. Further experimental research is required on non-α-cluster projectile-induced reactions, covering a range of target-projectile combinations to understand the reaction mechanism. At energies between 3 to 7 MeV/nucleon, the new experimental data may aid in improving the current theoretical models.

ACKNOWLEDGMENTS

The authors thank the BARC-TIFR Pelletron staff for their cooperation and help during the experiment. We also appreciate the support of our colleagues from the TASISPEC Lab, IIT Roorkee, India. H.S. acknowledges the MHRD Research Fellowship from the Government of India. We acknowledge the support of the Department of Atomic Energy, Government of India, under Project No. 12P-R&D-TFR-5.02-0300.

[1] B. B. Back, H. Esbensen, C. L. Jiang, and K. E. Rehm, Rev. Mod. Phys. **86**, 317 (2014).
[2] G. Wallerstein, I. Iben, Jr., P. Parker, A. M. Boesgaard, G. M. Hale, A. E. Champagne, C. A. Barnes, F. Käppeler, V. V. Smith *et al.*, Rev. Mod. Phys. **69**, 995 (1997).
[3] V. Jha, V. V. Parkar, and S. Kailas, Phys. Rep. **845**, 1 (2020).
[4] M. Dasgupta, D. J. Hinde, N. Rowley, and A. M. Stefanini, Annu. Rev. Nucl. Part. Sci. **48**, 401 (1998).
[5] C. L. Jiang, B. B. Back, K. E. Rehm, K. Hagino, G. Montagnoli, and A. M. Stefanini, Eur. Phys. J. A **57**, 235 (2021).
[6] K. E. Rehm, H. Esbensen, C. L. Jiang, B. B. Back, F. Borasi, B. Harss, R. V. F. Janssens, V. Nanal, J. Nolen, R. C. Pardo, M. Paul, P. Reiter, R. E. Segel, A. Sonzogni, J. Uusitalo, and A. H. Wuosmaa, Phys. Rev. Lett. **81**, 3341 (1998).
[7] D. Kumar, M. Maiti, and S. Lahiri, Phys. Rev. C **96**, 014617 (2017).
[8] A. Chauhan and M. Maiti, Phys. Rev. C **99**, 034608 (2019).
[9] R. Prajapat and M. Maiti, Phys. Rev. C **103**, 034620 (2021).
[10] R. Prajapat and M. Maiti, Phys. Rev. C **101**, 064620 (2020).
[11] R. Prajapat and M. Maiti, Phys. Rev. C **101**, 024608 (2020).
[12] R. Kumar, M. Maiti, T. N. Nag, and S. Sodaye, Phys. Rev. C **104**, 064606 (2021).
[13] M. K. Sharma, Unnati, B. K. Sharma, B. P. Singh, H. D. Bhardwaj, R. Kumar, K. S. Golda, and R. Prasad, Phys. Rev. C **70**, 044606 (2004).
[14] D. Singh, S. B. Linda, P. K. Giri, A. Mahato, R. Tripathi, H. Kumar, S. A. Tali, S. Parashari, A. Ali, R. Dubey *et al.*, Phys. Rev. C **97**, 064610 (2018).
[15] V. R. Sharma, P. P. Singh, Mohd. Shuaib, A. Yadav, I. Bala, M. K. Sharma, S. Gupta, D. P. Singh, R. Kumar, S. Murlithar *et al.*, Nucl. Phys. A **946**, 182 (2016).
[16] M. Cavinato, E. Fabrici, E. Gadioli, E. G. Erba, P. Vergani, M. Crippa, G. Colombo, I. Redaelli, and M. Ripamonti, Phys. Rev. C **52**, 2577 (1995).

[17] D. P. Singh, Unnati, P. P. Singh, A. Yadav, M. K. Sharma, B. P. Singh, K. S. Golda, R. Kumar, A. K. Sinha, and R. Prasad, Phys. Rev. C **80**, 014601 (2009).
[18] H. Kumar, S. A. Tali, M. A. Ansari, D. Singh, R. Ali, K. Kumar, N. P. M. Sathik, S. Parashari, A. Ali, R. Dubey *et al.*, Nucl. Phys. A **960**, 53 (2017).
[19] P. P. Singh, M. K. Sharma, Unnati, D. P. Singh, R. Kumar, K. S. Golda, B. P. Singh, and R. Prasad, Eur. Phys. J. A **34**, 29 (2007).
[20] A. Chauhan, M. Maiti, and S. Lahiri, Phys. Rev. C **99**, 064609 (2019).
[21] P. Kaur, M. Maiti, T. N. Nag, and S. Sodaye, Phys. Rev. C **105**, 014629 (2022).
[22] M. Sagwal, M. Maiti, T. N. Nag, and S. Sodaye, Eur. Phys. J. Plus **136**, 1057 (2021).
[23] S. Chakrabarty, B. S. Tomar, A. Goswami, G. K. Gubbi, S. B. Manohar, A. Sharma, B. Bindukumar, and S. Mukherjee, Nucl. Phys. A **678**, 355 (2000).
[24] S. A. Tali, H. Kumar, M. A. Ansari, A. Ali, D. Singh, R. Ali, P. K. Giri, S. B. Linda, R. Kumar, S. Parashari, S. Muralithar, and R. P. Singh, Phys. Rev. C **100**, 024622 (2019).
[25] I. M. Bhat, M. Shuaib, M. S. Asnain, V. R. Sharma, A. Yadav, M. K. Sharma, P. P. Singh, D. P. Singh, U. Gupta, R. N. Sahoo *et al.*, Nucl. Phys. A **1021**, 122421 (2022).
[26] M. S. Asnain, M. Shuaib, I. Majeed, M. K. Sharma, V. R. Sharma, A. Yadav, D. P. Singh, P. P. Singh, U. Gupta, R. N. Sahoo, A. Sood, M. Kaushik, S. Kumar, R. Kumar, B. P. Singh, and R. Prasad, Phys. Rev. C **104**, 034616 (2021).
[27] B. S. Tomar, A. Goswami, G. K. Gubbi, A. V. R. Reddy, S. B. Manohar, B. John, and S. K. Kataria, Phys. Rev. C **58**, 3478 (1998).
[28] R. Kumar, V. R. Sharma, A. Yadav, P. P. Singh, A. Agarwal, S. Appannababu, S. Mukherjee, B. P. Singh, R. Ali, and R. K. Bhowmik, Phys. Rev. C **96**, 054614 (2017).
[29] R. Tripathi, K. Sudarshan, S. Sodaye, and A. Goswami, J. Phys. G: Nucl. Part. Phys. **35**, 025101 (2008).
[30] M. Shuaib, V. R. Sharma, A. Yadav, P. P. Singh, M. K. Sharma, D. P. Singh, R. Kumar, R. P. Singh, S. Muralithar, B. P. Singh, and R. Prasad, Phys. Rev. C **94**, 014613 (2016).
[31] S. Kumar, P. K. Giri, R. Kumar, A. Yadav, R. Ali, S. Appannababu, A. Agarwal, S. Mukherjee, P. P. Singh, V. R. Sharma *et al.*, J. Phys. G: Nucl. Part. Phys. **49**, 105103 (2022).
[32] J. F. Ziegler, M. D. Ziegler, and J. P. Biersack, Nucl. Instrum. Methods Phys. Res. B **268**, 1818 (2010).
[33] National Nuclear Data Center, Brookhaven National Laboratory http://www.nndc.bnl.gov/nudat2/ (accessed on 06 February 2023).
[34] S. Y. F. Chu, L. P. Ekstrom, and R. B. Firestone, WWW Table of Radioactive Isotopes The Lund/LBNL Nuclear Data Search, 1999, http://nucleardata.nuclear.lu.se/toi/ (accessed on 06 February 2023).
[35] A. Gavron, Phys. Rev. C **21**, 230 (1980).
[36] M. Herman, R. Capote, B. V. Carlson, P. Oblozinsky, M. Sin, A. Trkov, H. Wienke, and V. Zerkin, Nucl. Data Sheets **108**, 2655 (2007).
[37] R. Bass, Phys. Rev. Lett. **39**, 265 (1977).
[38] C. M. Perey and F. G. Perey, At. Data Nucl. Data Tables **17**, 1 (1976).
[39] J. R. Huizenga and G. Igo, Nucl. Phys. **29**, 462 (1962).
[40] A. J. Sierk, Phys. Rev. C **33**, 2039 (1986).
[41] N. Bohr and J. W. Wheeler, Phys. Rev. **56**, 426 (1939).
[42] F. C. Williams, Nucl. Phys. A **166**, 231 (1971).
[43] C. H. Dasso and S. Landowne, Comput. Phys. Commun. **46**, 187 (1987).
[44] A. Gilbert and A. G. W. Cameron, Can. J. Phys. **43**, 1446 (1965).
[45] A. V. Ignatyuk, G. N. Smirenkin, and A. S. Tishin, Sov. J. Nucl. Phys. **21**, 255 (1975).
[46] A. D'Arrigo, G. Giardina, M. Herman, A. V. Ignatyuk, and A. Taccone, J. Phys. G: Nucl. Part. Phys. **20**, 365 (1994).
[47] P. G. Young, E. D. Arthur, M. Bozoian, T. R. England, G. M. Hale, R. J. LaBauve, R. C. Little, R. E. MacFarlane, D. G. Madland, R. T. Perry *et al.*, Trans. Am. Nucl. Soc. **60**, 271 (1989).
[48] A. S. Iljinov, M. V. Mebel, N. Bianchi, E. D. Sanctis, C. Guaraldo, V. Lucherini, V. Muccifora, E. Polli, A. R. Reolon, and P. Rossi, Nucl. Phys. A **543**, 517 (1992).
[49] R. Capote, M. Herman, P. Obložinský, P. G. Young, S. Goriely, T. Belgya, A. V. Ignatyuk, A. J. Koning, S. Hilaire, V. A. Plujko *et al.*, Nucl. Data Sheets **110**, 3107 (2009).
[50] A. J. Koning and J. P. Delaroche, Nucl. Phys. A **713**, 231 (2003).
[51] H. An and C. Cai, Phys. Rev. C **73**, 054605 (2006).
[52] F. D. Becchetti and G. W. Greenlees, Phys. Rev. **182**, 1190 (1969).
[53] V. Avrigeanu, P. E. Hodgson, and M. Avrigeanu, Phys. Rev. C **49**, 2136 (1994).
[54] R. D. Evans, *Atomic Nucleus* (McGraw-Hill, New York, 1995).
[55] C. Y. Wong, Phys. Rev. Lett. **31**, 766 (1973).
[56] Live Chart of Nuclides: Nuclear Structure and Decay Data, NDS, IAEA, 2019, https://www-nds.iaea.org/relnsd/vcharthtml/VChartHTML.html (accessed on 06 February 2023).
[57] WWW Chart of the Nuclides, Japanese Nuclear Data Library, 2014, https://wwwndc.jaea.go.jp/CN14/index.html (accessed on 06 February 2023).
[58] P. Misaelides, Radiochim. Acta **28**, 1 (1981).